The Astrophysical Journal Supplement Series, 268:47 (13pp), 2023 October https://doi.org/10.3847/1538-4365/acf0be


# Optical Constants of Martian Dust Analogs at UV–Visible–Near-infrared Wavelengths

Julia Martikainen[1,2], Olga Muñoz[1], Teresa Jardiel[3], Juan Carlos Gómez Martín[1], Marco Peiteado[3], Yannick Willame[4], Antti Penttilä[2], Karri Muinonen[2], Gerhard Wurm[5], and Tim Becker[5]
[1] Instituto de Astrofísica de Andalucía, CSIC, Granada, Spain
[2] University of Helsinki, Department of Physics, Helsinki, Finland
[3] Instituto de Cerámica y Vidrio, CSIC, Madrid, Spain
[4] Belgian Institute for Space Aeronomy (IASB-BIRA), Brussels, Belgium
[5] University of Duisburg-Essen, Faculty of Physics, Duisburg, Germany
*Received 2022 December 13; revised 2023 July 19; accepted 2023 August 14; published 2023 September 21*

## Abstract

We present an advanced light-scattering model to retrieve the optical constants of three Martian dust analogs: Johnson Space Center regolith simulant, Enhanced Mojave Mars Simulant, and Mars Global Simulant. The samples are prepared to have narrow particle-size distributions within the geometric-optics domain. We carry out laboratory measurements to obtain the particle-size distributions, shapes, and diffuse reflectance spectra of the Martian analogs deposited on a surface. Our model framework includes a ray-optics code to compute scattering properties for individual particles, and a radiative-transfer treatment to simulate the surface. The irregular shapes of the dust particles are taken into account in the model. We compare our derived imaginary parts of the refractive indices with those in the literature and find that they are much smaller than the ones that are commonly used for Martian dust. A sensitivity study shows that the retrieved optical constants are sensitive to the particle shape, which needs to be accounted for in applications that use different shapes. Finally, the derived values are validated by using them to reproduce the reflectance spectrum of the Martian surface regolith as observed by the Nadir and Occultation for Mars Discovery instrument on board the ExoMars mission.

*Unified Astronomy Thesaurus concepts:* Mars (1007); Computational methods (1965); Planetary surfaces (2113)

## 1. Introduction

Particle composition in light-scattering and radiative-transfer (RT) simulations is parameterized through the wavelength-dependent optical constants, the complex refractive indices ($m = n + ik$). The real part of the complex refractive index, $n$, describes the ratio of the speed of light in a vacuum to the phase velocity of light in the material, whereas the imaginary part, $k$, describes the absorption of light inside the material.

In Martian atmospheric studies, optical constants at UV–visible–near-infrared (NIR) wavelengths are needed in studies ranging from modeling single-particle scattering by the atmospheric dust to interpreting observed surface reflectance spectra and simulating the global Martian climate, which is why many works have solely focused on retrieving dust refractive indices. However, the connection between the airborne dust and surface regolith is not well understood. The Martian surface is known to have different particle-size distributions depending on the measurement location. Generally, dark regions contain larger particles (sizes ranging from 0.1 mm to 1 cm; Christensen & Moore 1992) than the bright regions (sizes below 100 $\mu$m; Ruff & Christensen 2002). Weitz et al. (2018) found that the size range of the particles at the Gale crater is 50–150 $\mu$m, whereas the Phoenix lander measured particle sizes from 20 to 100 $\mu$m (Goetz et al. 2010). Several studies have found that lifted dust contains smaller particles than the regolith, with particle effective radius ranging from 1 $\mu$m to occasionally exceeding 5 $\mu$m (Lemmon et al. 2019). The large variations in the particle-size distributions could potentially introduce compositional differences between the regolith and lifted dust that have to be accounted for when deriving dust optical properties. One of the first models to retrieve airborne dust refractive indices included Mie-scattering calculations using spherical particle shapes and the Mariner 9 ultraviolet spectra of the 1971 Mars dust storm (Pang et al. 1976). Their work was followed by Clancy et al. (1995) who applied the Hapke RT model (Hapke 2012) on palagonite-like dust mined at Maunakea, and by Ockert-Bell et al. (1997) who, likewise, utilized the Hapke model to reproduce spacecraft and ground-based observations. However, using the Hapke RT model to retrieve material optical properties poses a fundamental problem as the model parameters do not correspond to their physical counterparts, such as the particle sizes or roughness (Shepard & Helfenstein 2007). Later on, Tomasko et al. (1999) returned to spherical particles by simulating scattering by small particles through Mie computations, and by approximating scattering by large particles using a separate sum of diffraction, external reflection, and a parameterized function for internally transmitted light. To this day, the most widely used dust optical properties were retrieved by Wolff et al. (2009, 2010) from analyzing the observed dust storm spectra during the global dust event in 2007 at the 258–2900 nm region using cylindrical particle shapes. A recent study by Connour et al. (2022) followed suit by retrieving ultraviolet complex refractive indices using the same modeling approach as Wolff et al. (2009) together with the data from the Imaging Ultraviolet Spectrograph instrument on board the Mars Atmosphere and Volatile Evolution spacecraft. They further utilized surface-based derivations of the column-integrated optical depth from the Mastcam instrument on Curiosity.

Light-scattering computations are known to be sensitive to the particle sizes and shapes, therefore using unrealistic

**Table 1**
Bulk Major Element Chemistry (wt.%) for the JSC Mars-1, Enhanced Mojave Mars 2 (MMS-2), and Mars Global (MGS-1) Simulants

| Oxide | JSC Mars-1 | MMS-2 | MGS-1 |
|---|---|---|---|
| $SiO_2$ | 43.5 | 43.8 | 44.2 |
| $TiO_2$ | 3.8 | 0.8 | 0.6 |
| $Al_2O_3$ | 23.3 | 13.1 | 13.2 |
| $Cr_2O_3$ | … | <0.1 | … |
| $FeO_T$ | 15.6 | 18.4 | 11.5 |
| MnO | 0.3 | 0.1 | 0.1 |
| CaO | 6.2 | 8.0 | 7.6 |
| MgO | 3.4 | 6.7 | 15.0 |
| $Na_2O$ | 2.4 | 2.5 | 1.5 |
| $K_2O$ | 0.6 | 0.4 | 0.6 |
| $P_2O_5$ | 0.9 | 0.1 | 0.1 |
| $SO_3$ | … | 6.1 | … |
| LOI[a] | … | … | 5.5 |
| SUM | 100 | 100 | 100 |

**Note.**
[a] Loss on ignition.

particle-size distributions and/or shapes reflect heavily on the retrieved optical constants (see, e.g., Muñoz et al. 2021). The analysis of observational data requires the use of simplified model particles, such as spheres or cylinders, to reduce the number of free parameters. Several studies have shown that spherical shapes are oversimplified and do not represent the complexity of real dust grains well (see Arriaga et al. 2020; Duchêne et al. 2020). Furthermore, the calculated phase functions for a size distribution of cylinders produce a significant overestimation of the phase function near the backscattering direction when compared with observations of Martian dust (Wolff et al. 2010).

With these shortcomings in mind, we aim to better understand the role and impact of dust and clouds on the Martian atmosphere. Optical constants were retrieved for three Martian dust analogs by using an advanced light-scattering model that accounts for the complex shapes of the dust particles. All of the samples were well characterized: information on the particle shapes was obtained through field-emission scanning electron microscope (FESEM) images, and advanced processing routines were used to synthesize a narrow size distribution for each sample. With the help of the laboratory measurements, the only free parameter in the retrieval was the complex refractive index, which gives us an advantage when compared to previous retrievals that contain multiple free parameters. The derived optical constants were further validated by using them to reproduce the observed reflectance spectrum of Martian regolith. The paper is organized so that in Section 2 we introduce the Martian dust analogs and their size distributions. In Section 3, we go through the experimental setup and data. The optical constant retrieval together with a sensitivity study is presented in Section 4, and a comparison with the observed Nadir and Occultation for MArs Discovery (NOMAD) Ultraviolet and Visible Spectrometer (UVIS) surface spectrum in Section 5. Finally, summary and future prospects are viewed in Section 6.

## 2. Samples and Particle Sizes

Three Mars analogs relevant to the atmospheric dust on Mars were selected for this study: Johnson Space Center regolith simulant (JSC Mars-1), Enhanced Mojave Mars Simulant (MMS-2), and Mars Global Simulant (MGS-1). The three analogs provide a broad range of spectral variability. JSC Mars-1 (Allen et al. 1997) contains weathered volcanic ash from Pu'u Nene, a cinder cone located in Maunakea, Hawaii. The material is basaltic in nature and is recognized to simulate the bright regions on Mars well. MMS-2 is an enhanced Mars simulant developed by The Martian Garden.[6] The simulant represents the basaltic regions of Mars and is created by adding iron III oxide, magnesium oxide, sulfates, and silicates to the Jet Propulsion Laboratory's Mojave Mars Simulant (Peters et al. 2008) that consists of basaltic rock mined in the western Mojave desert. Whereas JSC Mars-1 contains glassy materials, MMS-2 is crystalline in texture. MGS-1 is an open standard designed to represent the well-characterized Rocknest wind-blown soil at Gale crater (Cannon et al. 2019). Unlike the JSC Mars-1 and MMS-2 simulants, the MGS-1 was created through mineralogy-based synthesis, where individual materials were mixed together from scratch. According to its developers, the MGS-1 standard is superior to the previous Martian analogs, as it was created after gaining more knowledge on the Martian regolith over the years. The major chemical components for all of the samples are presented in Table 1. Each simulant exhibits a different color as can be seen in Figure 1. The MMS-2 contains highly red material, the JSC Mars-1 is mostly brown with a hint of red, and the MGS-1 is dominated by gray-colored material.

As our model uses a code that works in the geometric-optics domain ($r \gg \lambda$), the JSC Mars-1, MMS-2, and MGS-1 simulants were processed to produce well-defined narrow size distributions between 20 and 40 $\mu$m in diameter. Figure 1 shows pictures of the final samples together with their FESEM images. To produce the size fractions desired, the samples were continuously checked for homogeneity and particle sizes. The as-received samples were placed on a sieve column with 200, 100, 63, 40, and 20 $\mu$m metal sieves. The powder that passed through the 40 $\mu$m sieve but did not make it through the 20 $\mu$m mesh was collected for the elaboration of the fraction. During the dry-screening process, smaller particles with larger specific surface areas (typically particles smaller than 5 $\mu$m in diameter) remained attached to the surfaces of the larger particles and thus did not pass through the sieve meshes. Therefore, in order to get rid of these tiny particles and to ensure that a narrow particle-size distribution was obtained, additional dispersion steps were necessary. A highly diluted amount of each powder fraction was ultrasonically dispersed for 2 minutes using an alcoholic solvent medium and adding a 0.3 wt.% of the polyelectrolyte dispersant Dolapix CE64 (Zschimmer & Schwarz). The sonicated material was then subjected to rapid decanting (time not exceeding 1 minute) after which the supernatant, containing not-yet-settled small particles, was removed. The sediment was redispersed and redecanted, and in the end a total of five consecutive sedimentations were necessary to achieve an optimal size separation. All fractions showed satisfactorily narrow size distributions and the corresponding FESEM images confirmed that after successive dispersion and sedimentation steps, the aforementioned tiny particles below 5 $\mu$m had effectively disengaged from the surfaces of the large particles and were no longer detectable. However, the same process for the MMS-2 analog led to a

[6] https://www.themartiangarden.com


**Figure 1.** The pictures and the FESEM images of the JSC Mars-1 20–40 $\mu$m fraction (first row), the MMS-2 20–40 $\mu$m fraction (second row), and the MGS-1 20–40 $\mu$m fraction (third row). The ruler intervals on the bottom right of the FESEM images are 20 $\mu$m and 10 $\mu$m.

distinct result. In this case, when running the programmed series of dispersions and sedimentations, the powder acquired a gradual change in color far from the characteristic red color of these powders. When analyzed by the X-ray diffraction analysis, it showed an abnormally high quantity of quartz, which was not at all comparable to the rest of the powders and fractions already obtained (Figure 2(c)). Visibly, below a certain size, the fractionation of this MMS-2 dust also results in a compositional separation, which is indicative of a certain size heterogeneity of the different phases in the starting powder. To avoid this problem, the as-received MMS-2 material was first milled (1 hr) in a tungsten-carbide (WC) planetary mill with WC balls and then subjected to the same separation and dispersion routine as described above. In this way, a new MMS-2 size fraction (between 20 and 40 $\mu$m) was produced, which now showed the characteristic reddish hue indicative of a higher compositional homogeneity (Figure 2(b)), and also displayed a narrow size distribution with no presence of tiny particles adhering to the large ones.

The particle-size distributions of the final JSC Mars-1 and MMS-2 samples were measured at the Instituto de Astrofísica de Andalucía with a laser light-scattering particle sizer (Malvern Mastersizer 2000), whereas the size distribution of the MGS-1 sample was obtained at the Instituto de Cerámica y Vidrio using a similar experimental setup. The detailed description of the particle sizer and the retrieval process can be found in Gómez Martín et al. (2020). Figure 3 shows the obtained projected surface area distributions $S(\log r)$ and number distributions $n(r)$. The particle sizer provides the distribution of surface-equivalent spheres, i.e., the radius of a sphere that has a projected surface area equal to the projected area of the nonspherical particle averaged over all directions. As the size distributions are monomodal, they can be characterized with their effective variances $v_{\rm eff}$, and radii $r_{\rm eff}$ (Hansen & Travis 1974):

$$r_{\rm eff} = \frac{\int_0^\infty r\pi r^2 n(r)dr}{\int_0^\infty \pi r^2 n(r)dr}, \quad (1)$$

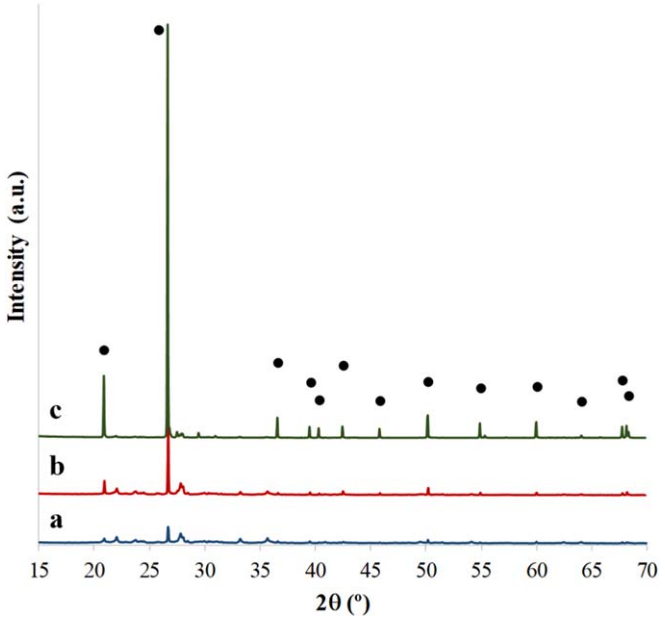


**Figure 2.** X-ray diffraction analyses of the MMS-2 analog: (a) dust as received, (b) 20–40 $\mu$m fraction (previously milled dust) and (c) 20–40 $\mu$m fraction (not milled dust); this last one showing an increased proportion of a quartz phase (black circles). $2\theta$ corresponds to the spacing between the crystals or atoms in the samples, determined by the angle of diffraction from the incident X-ray beam sent into the sample.

$$v_{\text{eff}} = \frac{\int_0^\infty (r - r_{\text{eff}})^2 \pi r^2 n(r) dr}{r_{\text{eff}}^2 \int_0^\infty \pi r^2 n(r) dr}. \quad (2)$$

The derived $r_{\text{eff}}$ and $v_{\text{eff}}$ for each sample are listed in Table 2.

## 3. Spectral Measurements

### 3.1. Setup

In this work, we derived optical constants from the diffuse reflectance spectra of the samples. Spectral measurements were carried out over the wavelength range of 200–2000 nm using a Varian Cary 5000 UV–visible–NIR integrating-sphere spectrophotometer at Centro de Instrumentación Científica, University of Granada. The instrument is equipped with a deuterium arc source for the UV wavelengths and a tungsten–halogen source for the visible–NIR region. The samples were deposited in a small bowl-shaped powder holder and gently compressed in such a way that they presented a flat surface to the incident light. Three measurement rounds of each sample were performed and each spectrum was calibrated using a polytetrafluoroethylene reflectance standard. The final spectrum was obtained by averaging the three measurement sets of the sample.

### 3.2. Measured Spectra

Figure 4 shows the diffuse reflectance spectra obtained for the simulants. The measurement uncertainties are wavelength dependent, not exceeding 15%. In this work, we have assumed the worst case uncertainty of 15% over the full wavelength range. The spectrum of the MMS-2 sample shows a steep red slope in the visible region with a ferric absorption band at around 800–1000 nm. A similar feature with a shallower slope can also be observed in the MGS-1 spectrum, whereas the JSC Mars-1 spectrum does not have a clear ferric absorption band.

**Table 2**
The Measured Effective Radii and Effective Variances of the Samples

| | $r_{\text{eff}}$ ($\mu$m) | $v_{\text{eff}}$ |
|---|---|---|
| JSC Mars-1 | 17.64 | 0.08 |
| MMS-2 | 18.02 | 0.08 |
| MGS-1 | 20.78 | 0.09 |

All of the spectra show artificial drops at around 770 nm that are caused by the spectrophotometer changing from one wavelength region to another. The spectrum of the MMS-2 sample continues to rise after the ferric absorption feature, while the JSC Mars-1 spectrum flattens. The MMS-2 sample shows a generally flat reflectance from 1100 to 2000 nm, whereas the reflectance of JSC Mars-1 slowly increases in the infrared. The MGS-1 sample exhibits a slow increase in the reflectance after the ferric feature until the spectrum becomes flat. When it comes to the level of reflectance, the MMS-2 simulant is much brighter than the other two simulants: the reflectance peaks at around 42% for the MMS-2, at around 21% for the MGS-1, and at around 19% for the JSC Mars-1.

The MMS-2 sample contains absorption features at 1400 and 1900 nm that are caused by OH and $H_2O$ (Allen et al. 1997). The 1900 nm band can also be seen in the JSC Mars-1 sample, however, the 1400 nm band is only visible in the MMS-2 spectrum. OH and $H_2O$ absorption features are absent in the Mars spectra implying that (1) the analogs are more wet than the regolith on Mars or (2) the features could be an effect of the laboratory conditions (higher humidity than on Mars).

## 4. Optical Constant Retrieval

### 4.1. Methods

The imaginary parts of the complex refractive indices, $k$, were derived using a method based on the retrieval by Martikainen et al. (2018). We upgraded the code to include particle-size distributions. The real part of the complex refractive index was fixed to 1.5 as it does not change significantly at the modeled wavelength region (see, e.g., Clancy et al. 1995; Tomasko et al. 1999; Wolff et al. 2009; Merikallio et al. 2013).

We carried out the retrieval with an optimization code that uses the measured diffuse reflectance spectra and the SIRIS4 (Muinonen et al. 2009; Lindqvist et al. 2018; Martikainen et al. 2018) ray tracer that simulates light scattering by Gaussian-random-sphere (GRS) particles larger than the wavelength of the incident light. In order to get rid of the noise, the measured spectra were smoothed out with a Savitzky–Golay filter in Python (see Figure 7). The shapes of the GRS particles are defined by the power-law index of the autocorrelation function of the logarithmic radial distance, $\nu_G$, and the standard deviation of the particle radius, $\sigma_G$ (Muinonen et al. 1996). In our model, we used $\nu_G = 3$ and $\sigma_G = 0.2$ so that the model particles (from now on GRS1) were qualitatively as realistic as possible (see Figure 5). The number of sample particles used for each run was 1000 and the number of rays was 100,000.

The computations were carried out as follows. First, we set upper ($k = 0.05$) and lower ($k = 0.0001$) limits for the $k$ so that the values create a broader range than what is usually assumed for the Martian dust in the literature. The bisection method was used to obtain a value inside the set boundaries for each wavelength. The retrieved $k$ was then entered as an input

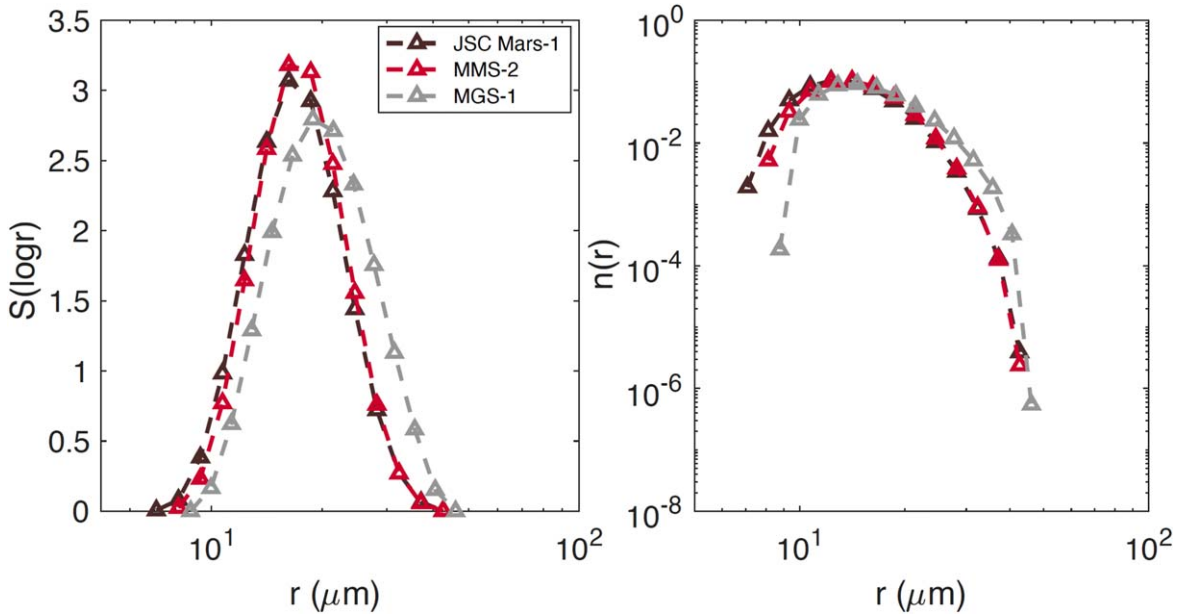


**Figure 3.** Projected surface area distributions (left) and number distributions (right) of the JSC Mars-1, the MMS-2, and the MGS-1 20–40 $\mu$m size fractions.

parameter into SIRIS4 to calculate the scattering properties for volume-equal GRS particles within the measured particle-size distribution. We further applied the Riemann sum to account for the different size bin widths. The computed scattering properties were then averaged over the size distribution and used as diffuse scatterers inside a vacuum to simulate the regolith. The retrieved reflectance was compared to the measured value of the reflectance spectrum, and the $k$ was iterated until the difference between the derived and the measured reflectance was less than 0.1% units of reflectance. As mentioned in Section 3, we assume the maximum uncertainty of 15% for the measured diffuse reflectance. The same procedure was carried out over the full spectral range. In Figure 6, we present an illustration of the model framework.

The optimization pipeline runs on MATLAB and further calls SIRIS4 that is coded with FORTRAN. The measured reflectance spectrum, upper and lower limits for $k$, and the size distribution were read from separate input files. Deriving $k$ for one wavelength took from 4 to 10 hr on a single CPU and the computations were run in parallel, four wavelengths at a time. The total computation time for all three samples was around 1200 hr using GRS1 shapes and $n = 1.5$.

### 4.2. Retrieved Refractive Indices

The refractive index retrieval was carried out for the wavelength range of 200–2000 nm with 25 nm steps from 200 to 400 nm and with 50 nm steps from 400 to 2000 nm. In Figure 7, we present the derived $k$ of the JSC Mars-1, MMS-2, and MGS-1 samples. Our results show that the derived $k$ for all three analogs falls in between 0.0001 and 0.0013 over the full wavelength range. All the values are listed in Table 3. The JSC Mars-1 analog is generally more absorbing than the other two analogs and has a narrow peak of absorption in the UV. The $k$ decreases rapidly until 700 nm and then steeply increases until 2000 nm. The MMS-2 is the brightest simulant in the NIR, and the smallest $k$ value 0.000135 was found at 1100 nm. A broad absorption peak is located below 500 nm and the $k$ values stay relatively flat in the infrared. Two small absorption bumps can

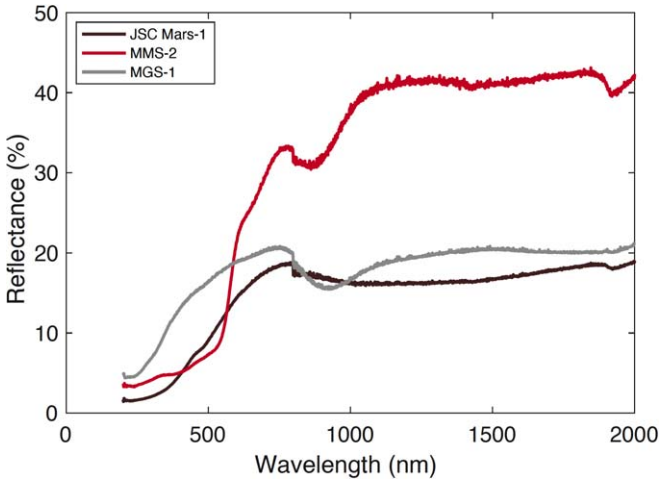


**Figure 4.** The diffuse reflectance spectra of the JSC Mars-1, MMS-2, and MGS-1 analogs.

be seen at around 800 nm and 1900 nm that can be linked to the ferric absorption band and to the $H_20$ absorption feature. The MGS-1 analog is somewhere between the JSC Mars-1 and MMS-2. It lacks a prominent absorption peak at shorter wavelengths but has a decrease in $k$ in the visible. Similar to the JSC Mars-1, the derived $k$ of the MGS-1 analog increases toward longer wavelengths. An absorption bump can be found at 900 nm around the ferric absorption band.

Generally, the derived $k$ for the three Martian analogs is smaller than those used for Martian dust in the literature derived from Martian remote-sensing and/or rover observations (e.g., Ockert-Bell et al. 1997; Wolff et al. 2006, 2009).

### 4.3. Sensitivity Study

#### 4.3.1. Real Part of the Refractive Index

As $n$ was fixed to 1.5 for the refractive index retrieval, we carried out sensitivity computations using $n = 1.4$ and $n = 1.6$ together with the GRS1 particles. The sensitivity study spans

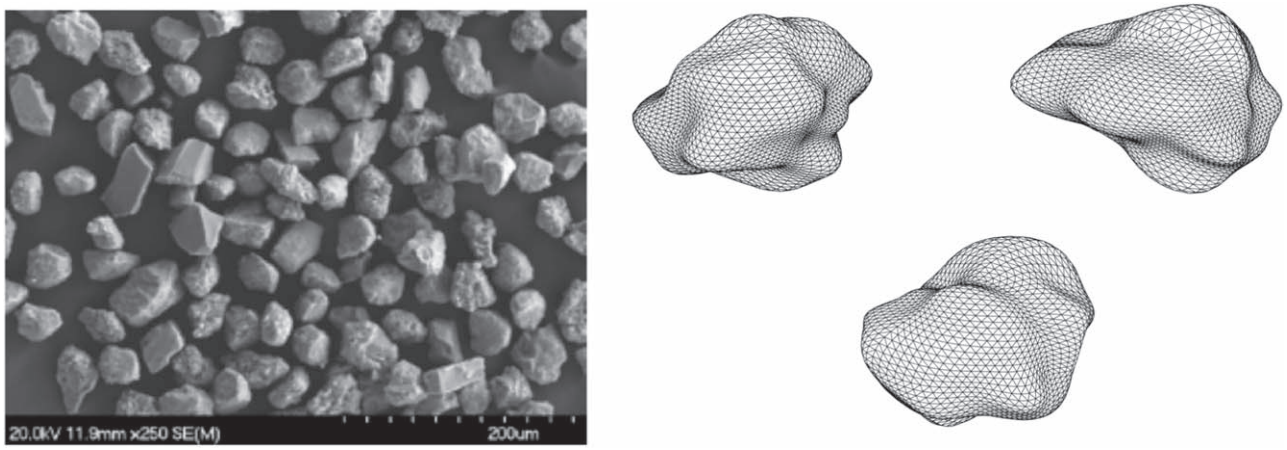


**Figure 5.** GRS1 particles used in the model (right) compared to the MMS-2 FESEM image (left).

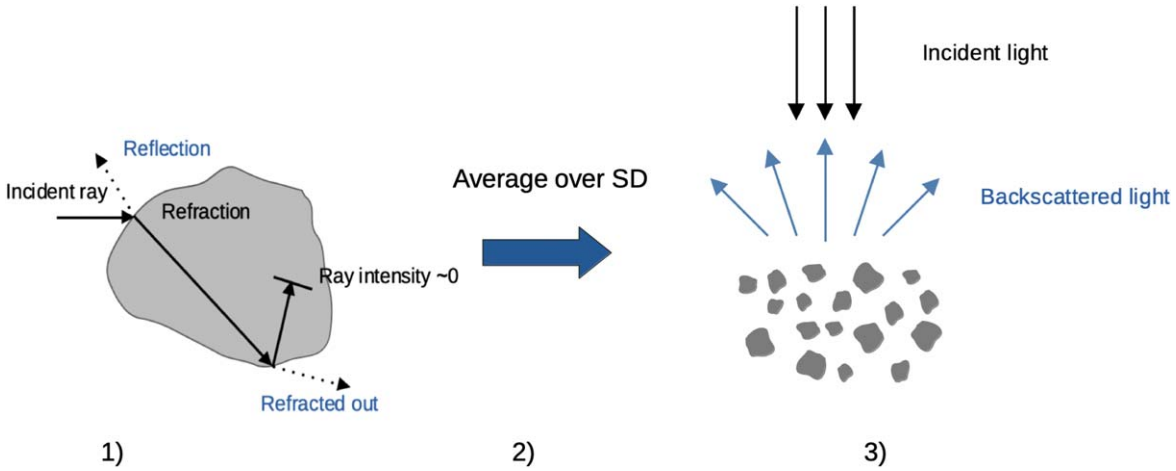


**Figure 6.** An illustration of the model for retrieving refractive indices. (1) Geometric optics is used to compute single-scattering properties of individual particle sizes, (2) the obtained single-scattering properties are averaged over the measured size distribution, (3) the regolith is simulated by using the averaged particles as diffuse scatterers in a vacuum.

over the full wavelength range (200–2000 nm). The results listed in Table 4 indicate that when changing the $n$ within the range of the typical values used for silicates, the retrieved $k$ values, and thus the computed reflectance, are not significantly affected: all the differences are within the uncertainty of the $k$.

#### 4.3.2. Particle Shape

Particle shape plays an important role in light-scattering simulations, which is why we included a sensitivity study for four different shapes. Apart from the previously used GRS1 particles, we utilized spheres, polyhedra, and spiky GRS shapes (from now on GRS2). The modeled shapes are shown in Figure 8. The spheres were selected due to their simplified shape and wide usage within the planetary science community, whereas the polyhedra shapes were utilized to study scattering by angular particles. Each polyhedron was created using convex hulls of the GRS1 particles as shown in Muinonen & Markkanen (2023). The GRS2 shapes were previously studied by Muñoz et al. (2007) who found that unrealistically spiky particles produced better fits against the measured scattering matrix of Libyan sand. They concluded that the spikiness mimics diffuse scattering by particles that contain wavelength-scale surface roughness. For the GRS2 particles, we set $\nu_G = 3.3$, and $\sigma_G = 0.2$. Furthermore, we set the minimum degree of the expansion of the power-law covariance function, $l_{\min}$, to 10 (see, e.g., Muinonen et al. 1996)

The derived $k$ values are presented in Table 5 for all four shapes. The wavelengths were selected to correspond to the NOMAD UVIS wavelength range of 400–650 nm. The retrieval for the GRS2 shapes was carried out over the full wavelength range from 200 to 2000 nm, and the obtained values are listed in Table 6. Figure 9 shows the retrieved $k$ values for all three analogs using GRS1 and GRS2 shapes. As a rule, the derived $k$ values increase when the particle irregularity increases: spherical shapes produce the smallest $k$ values, the spiky GRS2 shapes produce the largest $k$ values, whereas the GRS1 and polyhedral shapes produce similar $k$ values somewhere in between the spheres and GRS2 shapes. The differences between the $k$ values become more prominent with higher absorption. The reason behind the differences are due to rays escaping to infinity after shorter internal path lengths for the GRS2 particles. For the GRS2 particles, there is an increased preference toward the backscattering hemisphere because the interactions tend to take place, on average, more on the particle hemisphere facing the incoming light when compared to the other three particles shapes.

In Figure 10, we demonstrate how different shapes affect the computed spectra of the MMS-2 analog. The differences

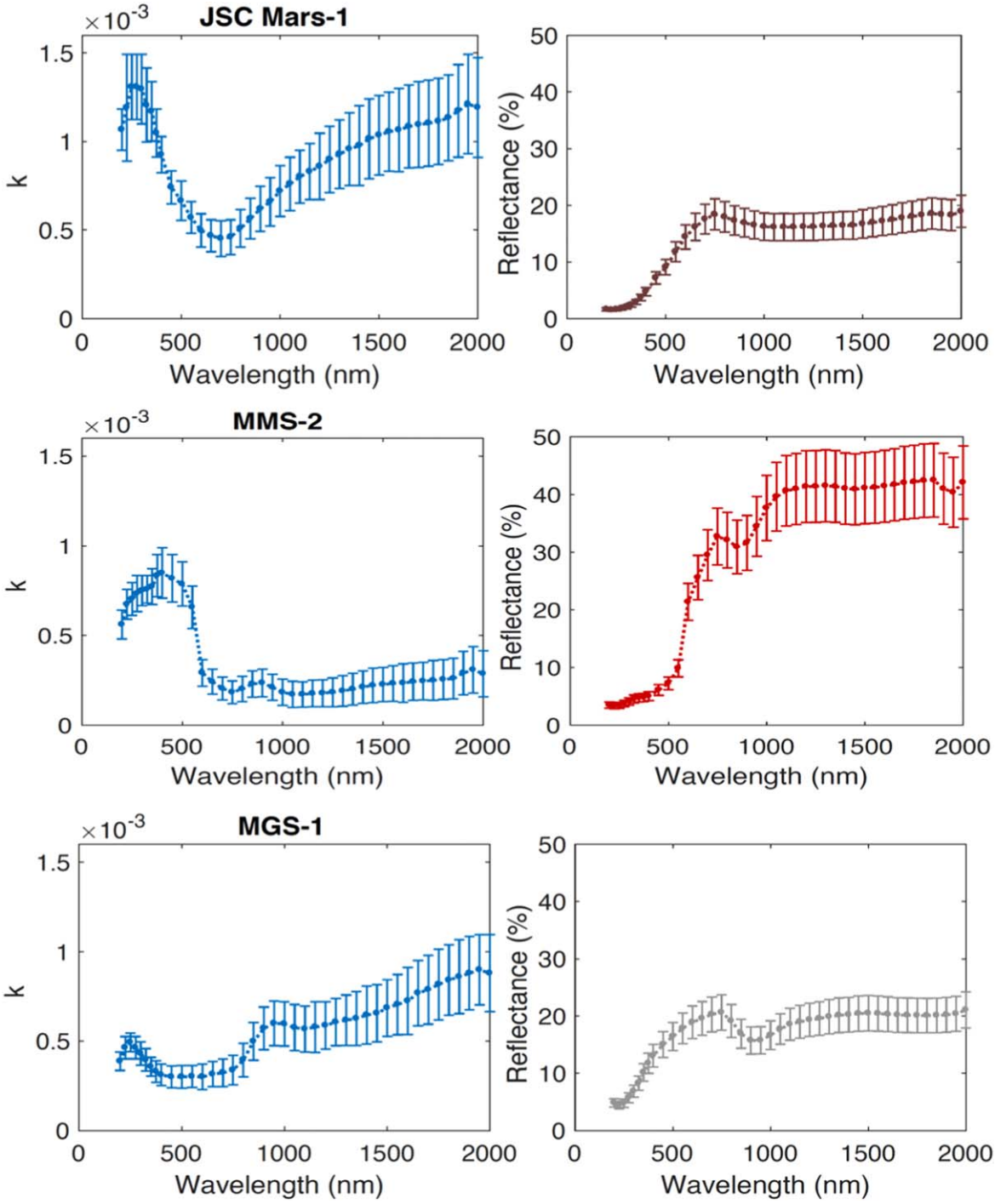


**Figure 7.** The derived imaginary parts of the refractive indices using GRS1 shapes and the smoothed-out diffuse reflectance spectra for the JSC Mars-1 (top), MMS-2 (middle), and MGS-1 (bottom) analogs.

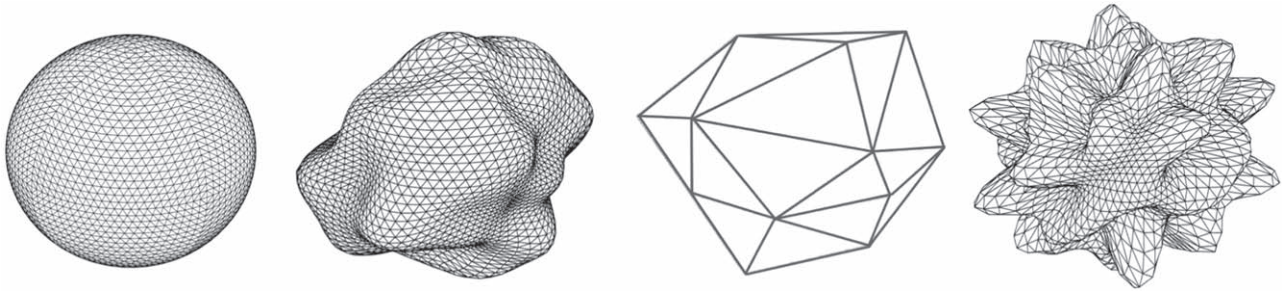

**Figure 8.** The shapes used in the sensitivity study. From left to right: sphere, GRS1, polyhedron, and GRS2.

**Table 3**
The Derived $k$ and the Uncertainties of the $k$ for the JSC Mars-1, MMS-2, and MGS-1 Samples Using the GRS1 Shapes

| $\lambda$ (nm) | $k_{JSC1}$ (GRS1) | $k_{MMS2}$ (GRS1) | $k_{MGS1}$ (GRS1) |
|---|---|---|---|
| 200 | 0.001067 ± 0.00012 | 0.000561 ± 0.00008 | 0.000387 ± 0.00005 |
| 225 | 0.001191 ± 0.00030 | 0.000674 ± 0.00008 | 0.000463 ± 0.00006 |
| 250 | 0.001308 ± 0.00018 | 0.000704 ± 0.00009 | 0.000493 ± 0.00005 |
| 275 | 0.001308 ± 0.00018 | 0.000734 ± 0.00010 | 0.000463 ± 0.00006 |
| 300 | 0.001296 ± 0.00020 | 0.000751 ± 0.00008 | 0.000431 ± 0.00007 |
| 325 | 0.001206 ± 0.00021 | 0.000758 ± 0.00008 | 0.000395 ± 0.00006 |
| 350 | 0.001170 ± 0.00017 | 0.000773 ± 0.00010 | 0.000357 ± 0.00005 |
| 375 | 0.001048 ± 0.00013 | 0.000834 ± 0.00012 | 0.000330 ± 0.00006 |
| 400 | 0.000926 ± 0.00010 | 0.000849 ± 0.00014 | 0.000311 ± 0.00006 |
| 450 | 0.000742 ± 0.00009 | 0.000819 ± 0.00013 | 0.000300 ± 0.00006 |
| 500 | 0.000666 ± 0.00011 | 0.000788 ± 0.00012 | 0.000300 ± 0.00006 |
| 550 | 0.000571 ± 0.00009 | 0.000658 ± 0.00012 | 0.000302 ± 0.00006 |
| 600 | 0.000498 ± 0.00010 | 0.000292 ± 0.00007 | 0.000300 ± 0.00007 |
| 650 | 0.000468 ± 0.00009 | 0.000243 ± 0.00007 | 0.000315 ± 0.00007 |
| 700 | 0.000452 ± 0.00010 | 0.000205 ± 0.00006 | 0.000323 ± 0.00008 |
| 750 | 0.000460 ± 0.00010 | 0.000184 ± 0.00006 | 0.000338 ± 0.00008 |
| 800 | 0.000510 ± 0.00011 | 0.000202 ± 0.00007 | 0.000394 ± 0.00009 |
| 850 | 0.000565 ± 0.00012 | 0.000230 ± 0.00007 | 0.000498 ± 0.00011 |
| 900 | 0.000620 ± 0.00013 | 0.000236 ± 0.00008 | 0.000571 ± 0.00012 |
| 950 | 0.000660 ± 0.00014 | 0.000212 ± 0.00007 | 0.000599 ± 0.00013 |
| 1000 | 0.000721 ± 0.00014 | 0.000184 ± 0.00007 | 0.000596 ± 0.00012 |
| 1050 | 0.000761 ± 0.00015 | 0.000172 ± 0.00007 | 0.000575 ± 0.00013 |
| 1100 | 0.000802 ± 0.00015 | 0.000172 ± 0.00007 | 0.000567 ± 0.00013 |
| 1150 | 0.000831 ± 0.00016 | 0.000177 ± 0.00007 | 0.000578 ± 0.00014 |
| 1200 | 0.000860 ± 0.00019 | 0.000179 ± 0.00008 | 0.000587 ± 0.00013 |
| 1250 | 0.000899 ± 0.00019 | 0.000184 ± 0.00008 | 0.000606 ± 0.00013 |
| 1300 | 0.000929 ± 0.00019 | 0.000191 ± 0.00008 | 0.000616 ± 0.00014 |
| 1350 | 0.000958 ± 0.00020 | 0.000201 ± 0.00009 | 0.000626 ± 0.00015 |
| 1400 | 0.000977 ± 0.00022 | 0.000213 ± 0.00009 | 0.000645 ± 0.00016 |
| 1450 | 0.001016 ± 0.00022 | 0.000222 ± 0.00010 | 0.000655 ± 0.00016 |
| 1500 | 0.001036 ± 0.00022 | 0.000227 ± 0.00010 | 0.000685 ± 0.00016 |
| 1550 | 0.001056 ± 0.00022 | 0.000233 ± 0.00010 | 0.000704 ± 0.00017 |
| 1600 | 0.001065 ± 0.00023 | 0.000235 ± 0.00011 | 0.000724 ± 0.00019 |
| 1650 | 0.001085 ± 0.00023 | 0.000243 ± 0.00010 | 0.000768 ± 0.00018 |
| 1700 | 0.001095 ± 0.00024 | 0.000246 ± 0.00011 | 0.000787 ± 0.00019 |
| 1750 | 0.001104 ± 0.00024 | 0.000250 ± 0.00011 | 0.000816 ± 0.00020 |
| 1800 | 0.001114 ± 0.00024 | 0.000255 ± 0.00011 | 0.000841 ± 0.00020 |
| 1850 | 0.001134 ± 0.00024 | 0.000260 ± 0.00011 | 0.000860 ± 0.00021 |
| 1900 | 0.001173 ± 0.00026 | 0.000291 ± 0.00012 | 0.000880 ± 0.00021 |
| 1950 | 0.001212 ± 0.00028 | 0.000309 ± 0.00013 | 0.000899 ± 0.00020 |
| 2000 | 0.001192 ± 0.00028 | 0.000287 ± 0.00013 | 0.000880 ± 0.00022 |

decrease with higher absorption as the computed reflectance becomes less sensitive to the changes in the $k$ values. When selecting the $k$ values that best represent the sample, it is important to account for as much experimental data as possible. Even though the shapes of the GRS1 particles resemble the overall features of the measured dust particles, they do not include wavelength-scale surface roughness that can be clearly seen in the Figure 1 FESEM images. Based on the previous studies, spiky GRS2 particles mimic the surface roughness and can produce good fits to the measured scattering matrices of dust. Therefore, the optical model using GRS2 particles should be considered over the one that uses the GRS1 particles as it can better reproduce the experimental data.

## 5. Comparison with Observations

### 5.1. Observations

In order to understand how well our Martian analogs represent the Martian surface, we used the new set of refractive indices for the Martian dust to reproduce the UVIS spectrum of the Martian regolith observed by the NOMAD instrument at the 400–600 nm wavelength range (see Willame et al. 2022). We selected observations with minimal impact from the atmosphere: they were carried out above a relatively high-visible-albedo region at Elysium Planitia when there were no ice clouds, the amount of dust was low, and the solar zenith angle was small (the angle between the Sun's rays and the zenith). The observed spectrum is shown in Figure 11. Seasonal dust storms originating from Elysium Planitia are common (Cantor et al. 2019) and thus it is reasonable to assume that the regolith in this region contributes to the dust observed in the atmosphere.

### 5.2. Methods

The modeling approach to simulate Martian regolith was similar to the one presented in Section 4.1. First, the single-scattering properties of individual particle sizes were computed using the geometric-optics code SIRIS4 and the derived complex refractive indices. The computed scattering properties

**Table 4**
The Derived $k$ for the JSC Mars-1, MMS-2, and MGS-1 Analogs Using GRS1 Shapes with $n = 1.4$, $n = 1.5$, and $n = 1.6$

| | $\lambda$ (nm) | $n = 1.4$ | $n = 1.5$ | $n = 1.6$ |
|---|---|---|---|---|
| JSC Mars-1 | 200 | 0.000946 | 0.001067 | 0.001138 |
| | 300 | 0.001211 | 0.001296 | 0.001467 |
| | 400 | 0.000864 | 0.000926 | 0.000956 |
| | 450 | 0.000712 | 0.000742 | 0.000742 |
| | 500 | 0.000651 | 0.000666 | 0.000666 |
| | 550 | 0.000552 | 0.000571 | 0.000559 |
| | 600 | 0.000483 | 0.000498 | 0.000483 |
| | 650 | 0.000460 | 0.000468 | 0.000460 |
| | 1000 | 0.000709 | 0.000721 | 0.000709 |
| | 1250 | 0.000904 | 0.000899 | 0.000880 |
| | 1500 | 0.001028 | 0.001036 | 0.001017 |
| | 1750 | 0.001096 | 0.001104 | 0.001085 |
| | 2000 | 0.001183 | 0.001192 | 0.001163 |
| MMS-2 | 200 | 0.000523 | 0.000561 | 0.000583 |
| | 300 | 0.000719 | 0.000751 | 0.000783 |
| | 400 | 0.000819 | 0.000849 | 0.000864 |
| | 450 | 0.000803 | 0.000819 | 0.000834 |
| | 500 | 0.000773 | 0.000788 | 0.000788 |
| | 550 | 0.000643 | 0.000658 | 0.000658 |
| | 600 | 0.000292 | 0.000292 | 0.000284 |
| | 650 | 0.000245 | 0.000243 | 0.000239 |
| | 1000 | 0.000184 | 0.000184 | 0.000178 |
| | 1250 | 0.000189 | 0.000184 | 0.000182 |
| | 1500 | 0.000230 | 0.000227 | 0.000221 |
| | 1750 | 0.000255 | 0.000250 | 0.000238 |
| | 2000 | 0.000289 | 0.000287 | 0.000273 |
| MGS-1 | 200 | 0.000372 | 0.000387 | 0.000402 |
| | 300 | 0.000420 | 0.000431 | 0.000442 |
| | 400 | 0.000308 | 0.000311 | 0.000311 |
| | 450 | 0.000300 | 0.000300 | 0.000300 |
| | 500 | 0.000300 | 0.000300 | 0.000294 |
| | 550 | 0.000296 | 0.000302 | 0.000292 |
| | 600 | 0.000300 | 0.000300 | 0.000296 |
| | 650 | 0.000311 | 0.000315 | 0.000308 |
| | 1000 | 0.000590 | 0.000596 | 0.000587 |
| | 1250 | 0.000597 | 0.000606 | 0.000587 |
| | 1500 | 0.000675 | 0.000685 | 0.000665 |
| | 1750 | 0.000811 | 0.000816 | 0.000802 |
| | 2000 | 0.000860 | 0.000880 | 0.000841 |

were then averaged over a size distribution and used as input in the next computational step. In Section 4.1, SIRIS4 was used to simulate the sample measured by the integrating-sphere spectrophotometer by calculating the total reflectance of the surface with the initial rays coming directly from above the surface mimicking the reflectance spectra experimental setup. In the case of NOMAD observations, bidirectional reflectance computations were needed as the sunlight comes from a solar zenith angle and the reflectance is measured at a specific phase angle. Therefore, we utilized the so-called Radiative Transfer and Coherent Backscattering (RT-CB) code, which is a Monte Carlo RT solver (Muinonen 2004). Taking into account CB requires the amplitude matrices of the scatterers as an input, which was not possible as SIRIS4 can only produce Mueller matrices. However, the contribution from CB is negligible at the phase angle of the observations, thus it can be omitted in our model. The regolith is simulated with plane geometry by using a thick slab that does not let any rays through. Following

**Table 5**
The Derived $k$ for the JSC Mars-1, MMS-2, and MGS-1 Analogs Using Spheres, GRS1, Polyhedra, and GRS2 Shapes

| | $\lambda$ (nm) | Sphere | GRS1 | Polyhedra | GRS2 |
|---|---|---|---|---|---|
| JSC Mars-1 | 400 | 0.000651 | 0.000926 | 0.000926 | 0.001292 |
| | 450 | 0.000514 | 0.000742 | 0.000758 | 0.001017 |
| | 500 | 0.000452 | 0.000666 | 0.000666 | 0.000926 |
| | 550 | 0.000384 | 0.000571 | 0.000578 | 0.000773 |
| | 600 | 0.000330 | 0.000498 | 0.000510 | 0.000681 |
| | 650 | 0.000315 | 0.000468 | 0.000481 | 0.000643 |
| MMS-2 | 400 | 0.000620 | 0.000849 | 0.000869 | 0.001200 |
| | 450 | 0.000575 | 0.000819 | 0.000842 | 0.001139 |
| | 500 | 0.000544 | 0.000788 | 0.000815 | 0.001093 |
| | 550 | 0.000452 | 0.000658 | 0.000669 | 0.000910 |
| | 600 | 0.000193 | 0.000292 | 0.000304 | 0.000407 |
| | 650 | 0.000159 | 0.000243 | 0.000250 | 0.000338 |
| MGS-1 | 400 | 0.000210 | 0.000311 | 0.000320 | 0.000430 |
| | 450 | 0.000201 | 0.000300 | 0.000311 | 0.000414 |
| | 500 | 0.000201 | 0.000300 | 0.000306 | 0.000416 |
| | 550 | 0.000201 | 0.000302 | 0.000307 | 0.000416 |
| | 600 | 0.000199 | 0.000300 | 0.000309 | 0.000414 |
| | 650 | 0.000208 | 0.000315 | 0.000320 | 0.000433 |

**Note.** The real part of the refractive index was fixed to 1.5.

the observations, we set the initial angle (solar zenith angle) to 16°.5 and retrieved the reflectance at a 16°.8 phase angle.

### 5.3. Martian Regolith

For this study, it was important to understand how well the three Martian dust analogs represent the Martian regolith. We carried out bidirectional reflectance computations using the derived refractive indices of the GRS2 particles and the modeling approach presented in Section 5.2 using GRS2 shapes. Particle-size distributions of the Martian regolith are poorly known, therefore we used the 20–40 $\mu$m narrow size distribution as a first guess for the dust analogs. The results of the computations are presented in Figure 11. The uncertainties of the NOMAD UVIS spectrum are within 2.6%–4.3% (including random and systematic errors). The uncertainties of the computed reflectances are around 0.1% (units of reflectance) at each wavelength. We found that the 20–40 $\mu$m narrow size distribution produced spectra relatively close to the NOMAD observations. Out of the three Martian dust analogs, the spectrum of the MMS-2 analog best resembles the observed regolith spectrum showing a distinct steep red slope in the visible, whereas the spectra of the other two analogs are too flat compared to the NOMAD UVIS spectrum.

Particle-size distributions on planetary surfaces are known to be broad. Several studies (see, e.g., Ruff & Christensen 2002) suggest that the regolith particle sizes in bright Martian regions are below 100 $\mu$m in diameter, some even predicting these areas to contain fine-grained sand in the size range of 2–40 $\mu$m (Christensen 1986). To better simulate the surface, we assumed power-law size distributions in the range of 2–40 $\mu$m (in diameter) and repeated the bidirectional reflectance computations for the MMS-2 analog (see Figure 12). The best match between the computed and observed spectra was found qualitatively when using a power-law index 1.5. This result supports the thermal observations of Martian regolith by Christensen (1986). We note that in the UV the observed

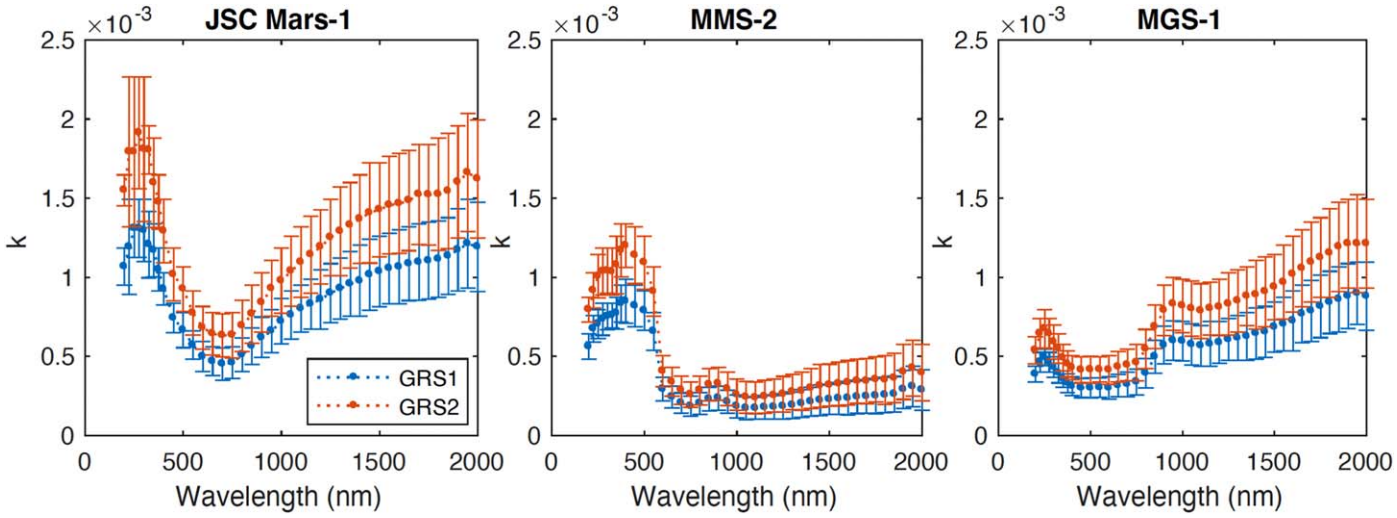


**Figure 9.** The derived $k$ values of the JSC Mars-1, MMS-2, and MGS-1 samples using GRS1 and GRS2 shapes.

**Table 6**
The Derived $k$ and the Uncertainties of the $k$ for the JSC Mars-1, MMS-2, and MGS-1 Samples Using the GRS2 Shapes

| $\lambda$ (nm) | $k_{\mathrm{JSC1}}$ (GRS2) | $k_{\mathrm{MMS2}}$ (GRS2) | $k_{\mathrm{MGS1}}$ (GRS2) |
|---|---|---|---|
| 200 | 0.001550 ± 0.00010 | 0.000795 ± 0.00008 | 0.000538 ± 0.00008 |
| 225 | 0.001792 ± 0.00047 | 0.000916 ± 0.00011 | 0.000644 ± 0.00009 |
| 250 | 0.001792 ± 0.00047 | 0.001006 ± 0.00014 | 0.000674 ± 0.00012 |
| 275 | 0.001913 ± 0.00035 | 0.001036 ± 0.00015 | 0.000644 ± 0.00009 |
| 300 | 0.001809 ± 0.00046 | 0.001040 ± 0.00014 | 0.000591 ± 0.00011 |
| 325 | 0.001804 ± 0.00015 | 0.001035 ± 0.00015 | 0.000549 ± 0.00009 |
| 350 | 0.001597 ± 0.00028 | 0.001078 ± 0.00018 | 0.000491 ± 0.00008 |
| 375 | 0.001475 ± 0.00017 | 0.001170 ± 0.00017 | 0.000452 ± 0.00008 |
| 400 | 0.001292 ± 0.00020 | 0.001200 ± 0.00014 | 0.000430 ± 0.00008 |
| 450 | 0.001017 ± 0.00017 | 0.001139 ± 0.00018 | 0.000414 ± 0.00008 |
| 500 | 0.000926 ± 0.00014 | 0.001093 ± 0.00017 | 0.000416 ± 0.00009 |
| 550 | 0.000773 ± 0.00014 | 0.000910 ± 0.00016 | 0.000416 ± 0.00008 |
| 600 | 0.000681 ± 0.00013 | 0.000407 ± 0.00010 | 0.000414 ± 0.00009 |
| 650 | 0.000643 ± 0.00013 | 0.000338 ± 0.00009 | 0.000433 ± 0.00010 |
| 700 | 0.000632 ± 0.00014 | 0.000287 ± 0.00009 | 0.000445 ± 0.00010 |
| 750 | 0.000634 ± 0.00014 | 0.000258 ± 0.00008 | 0.000460 ± 0.00011 |
| 800 | 0.000693 ± 0.00016 | 0.000285 ± 0.00009 | 0.000547 ± 0.00012 |
| 850 | 0.000767 ± 0.00018 | 0.000321 ± 0.00010 | 0.000687 ± 0.00014 |
| 900 | 0.000840 ± 0.00019 | 0.000327 ± 0.00010 | 0.000791 ± 0.00016 |
| 950 | 0.000929 ± 0.00018 | 0.000294 ± 0.00011 | 0.000831 ± 0.00017 |
| 1000 | 0.000978 ± 0.00021 | 0.000257 ± 0.00010 | 0.000819 ± 0.00017 |
| 1050 | 0.001039 ± 0.00022 | 0.000242 ± 0.00010 | 0.000801 ± 0.00017 |
| 1100 | 0.001095 ± 0.00022 | 0.000238 ± 0.00010 | 0.000787 ± 0.00017 |
| 1150 | 0.001143 ± 0.00024 | 0.000245 ± 0.00010 | 0.000802 ± 0.00017 |
| 1200 | 0.001192 ± 0.00023 | 0.000252 ± 0.00010 | 0.000811 ± 0.00018 |
| 1250 | 0.001251 ± 0.00024 | 0.000260 ± 0.00011 | 0.000831 ± 0.00020 |
| 1300 | 0.001290 ± 0.00028 | 0.000274 ± 0.00011 | 0.000850 ± 0.00020 |
| 1350 | 0.001329 ± 0.00027 | 0.000279 ± 0.00012 | 0.000880 ± 0.00019 |
| 1400 | 0.001368 ± 0.00028 | 0.000298 ± 0.00013 | 0.000889 ± 0.00022 |
| 1450 | 0.001407 ± 0.00032 | 0.000313 ± 0.00013 | 0.000909 ± 0.00022 |
| 1500 | 0.001427 ± 0.00030 | 0.000318 ± 0.00013 | 0.000938 ± 0.00021 |
| 1550 | 0.001456 ± 0.00031 | 0.000326 ± 0.00014 | 0.000968 ± 0.00023 |
| 1600 | 0.001466 ± 0.00032 | 0.000333 ± 0.00014 | 0.001019 ± 0.00024 |
| 1650 | 0.001485 ± 0.00032 | 0.000343 ± 0.00014 | 0.001056 ± 0.00024 |
| 1700 | 0.001524 ± 0.00032 | 0.000343 ± 0.00014 | 0.001095 ± 0.00025 |
| 1750 | 0.001522 ± 0.00032 | 0.000353 ± 0.00014 | 0.001124 ± 0.00025 |
| 1800 | 0.001524 ± 0.00036 | 0.000351 ± 0.00016 | 0.001153 ± 0.00028 |
| 1850 | 0.001544 ± 0.00036 | 0.000362 ± 0.00016 | 0.001192 ± 0.00028 |
| 1900 | 0.001602 ± 0.00035 | 0.000401 ± 0.00017 | 0.001212 ± 0.00028 |
| 1950 | 0.001661 ± 0.00037 | 0.000426 ± 0.00018 | 0.001212 ± 0.00031 |
| 2000 | 0.001622 ± 0.00037 | 0.000396 ± 0.00018 | 0.001212 ± 0.00028 |

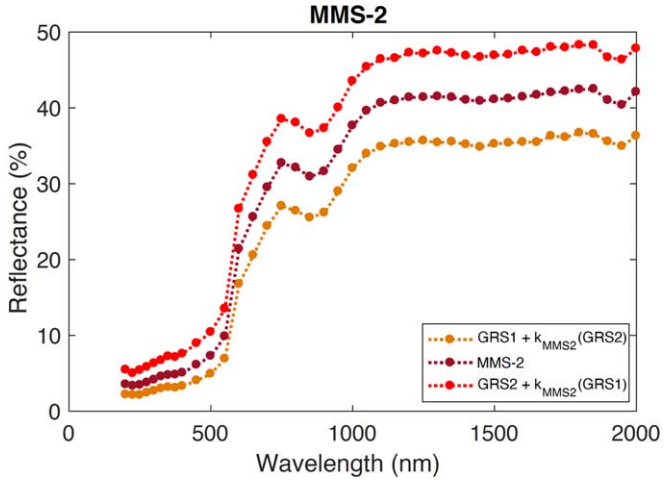


**Figure 10.** The measured reflectance of the MMS-2 sample compared to the computed spectra using the GRS1 shapes with the retrieved $k_{MMS2}$ (GRS2) and the GRS2 shapes with the $k_{MMS2}$ (GRS1).

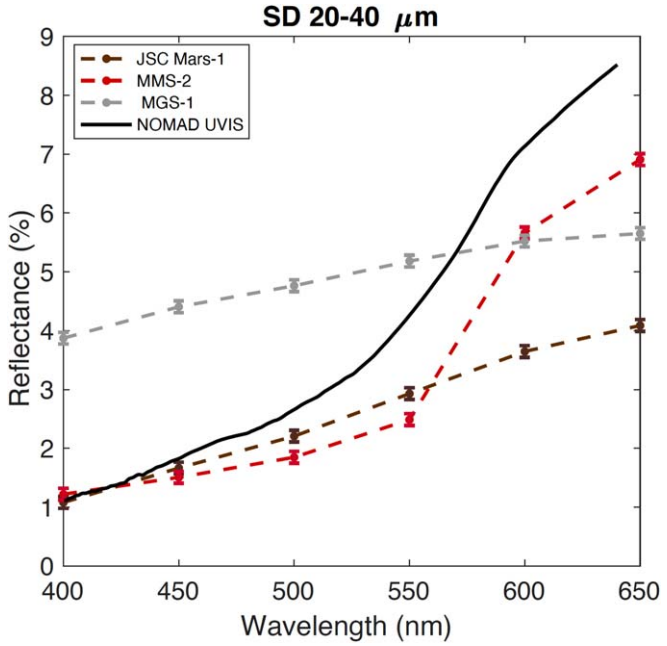


**Figure 11.** The observed NOMAD UVIS spectrum compared to the computed bidirectional reflectance spectra using the 20–40 $\mu$m narrow size distribution and the previously derived $k$ (GRS2) of the three Martian dust analogs.

spectrum has a slightly steeper slope than the analog spectrum, however, the overall fit is good. In order to better model the UV region, a Martian analog showing higher absorption in the UV should be considered in future work.

It is not clear how well lifted dust represents the surface in terms of composition. For comparison, we repeated the bidirectional reflectance computations using our advanced light-scattering model together with the optical constants retrieved by Wolff et al. (2009) from dust storm observations. The power-law index was fixed to 3 for a particle-size range of 2–40 $\mu$m. The computations produced a dark spectrum that does not match well with the regolith observations. Similarly to the MMS-2 analog, the computed spectrum in the UV is too flat when compared to the observations. In order to produce a spectrum with a level that matches better with the observations, the amount of small particles would have to be substantially increased while larger particles would have to be omitted. This is not realistic as the Martian regolith consists of a wide size range of particles. A possible explanation for the differences between our derived optical constants and those of Wolff et al. (2009) could be that the dust storm observations used by Wolff et al. (2009) were of dust from a different region than the observed area that we used. In addition, the particle-size distributions have not been measured during the dust storm observations, which can cause large uncertainties to the retrieved $k$ values if assumed incorrectly. Compositional differences between the airborne dust and surface regolith are not well known and can contribute to the results. The compositional separation that was seen when producing samples below a certain size (see Section 2) could be operating on Mars to some extent. We also note that the $k$ values retrieved by Wolff et al. (2009) were obtained from using cylinders. As shown in Section 4.3.2, the derived $k$ values are sensitive to the particle shape. Further investigation is needed to understand the discrepancies.

Modeling the Martian surface is challenging, since the particle-size distributions of the regolith and the atmospheric effects on the surface reflectance observed from space are not well known. The current model approximates particle sizes based on previous studies and omits the effects of the atmosphere. Nevertheless, the preliminary bidirectional reflectance computations show that our Martian dust analogs, especially the MMS-2 simulant, represent the observed regolith well in the NOMAD spectral range.

## 6. Summary and Conclusions

There is a high demand for realistic optical constants for Martian dust as they are a vital component in scattering and RT models. For the first time, we present a retrieval that is supported by direct laboratory measurements and realistic particle shapes.

We introduced a new model framework to retrieve the imaginary parts of the complex refractive indices, $k$, for three Martian dust analogs: JSC Mars-1, MMS-2, and MGS-1. The retrieval was based on an advanced light-scattering model and the measured reflectance spectra, the measured particle-size distributions, and the FESEM images of the samples. In the model, we accounted for the irregular shapes of the dust grains by using GRS particles. The retrieved $k$ over the 200–2000 nm wavelength range was found to be much smaller than those in the literature for airborne dust. The differences can partly be explained by the choice of particle shapes: real dust particles consist of a variety of different irregular shapes. We have used an ensemble of 1000 sample particles with realistic shapes for each wavelength, whereas previous studies have utilized spheres or a cylindrical shape with a diameter-to-length ratio of 1 over the full wavelength range. Our model is based on advanced light-scattering methods, and the particle-size distributions, shapes, and reflectance spectra were well constrained through laboratory measurements. Retrieval of the $k$ values from observations is far more challenging due to the lack of information on, e.g., particle sizes and shapes. We note that compositional differences between the regolith and lifted dust are poorly understood and could contribute to the discrepancies between the $k$ values retrieved from dust storm observations and the $k$ values retrieved using large particle-size distributions. To further validate our results, we proved that, in

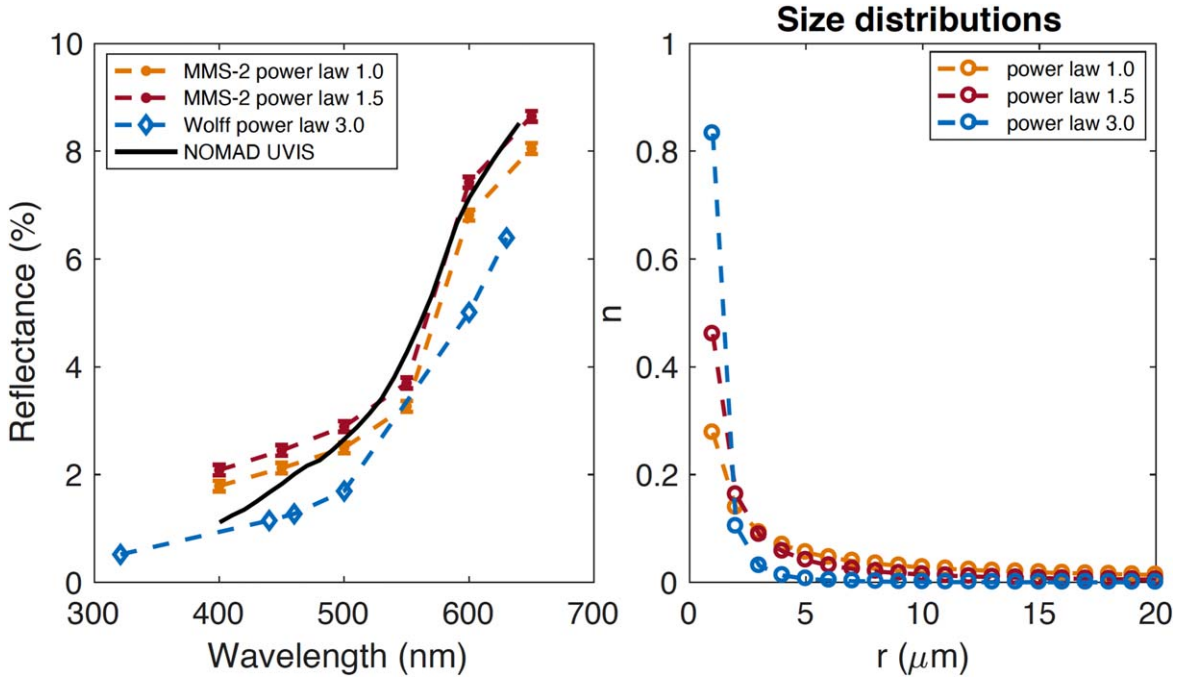


**Figure 12.** In the left panel, we present the NOMAD UVIS spectrum and the computed bidirectional reflectance spectra for the MMS-2 analog using power-law size distributions with power-law indices 1.0 and 1.5 in the range of 2–40 $\mu$m. Furthermore, we present the bidirectional reflectance spectrum computed by using the optical constants of Wolff et al. (2009) and a power-law size distribution with index 3.0. The right panel shows the number distributions.

the range of 400–650 nm, it was possible to reproduce the observed spectrum of a bright surface region by using the derived $k$ and a particle-size range supported by a previous study (see Christensen 1986).

In the sensitivity study presented in Section 4.3, we concluded that the real part of the complex refractive index, $n$, does not have a significant impact on the derived $k$ values when carrying out a retrieval from a measured reflectance spectrum. Further, the $k$ retrieval is sensitive to the particle shape: when the particle irregularity increases the obtained $k$ values increase. Choosing an optical model that best represents the dust becomes challenging as the optical properties are dependent on the particle shape. Thus, experimental data is in the key role: based on a previous study by Muñoz et al. (2007), spiky GRS2 shapes (presented in Table 6) are more realistic for reproducing the scattering pattern of Martian dust and should therefore be considered over smoother particle shapes.

Currently, all the retrievals are based on analog samples or spectral observations affected by the atmosphere. Even though the analogs are created to resemble different surface regions as closely as possible, they do not match the observations perfectly. For a more accurate retrieval, it is essential to obtain particle-size distributions and diffuse reflectance measurements of the regolith taken on the surface or through a sample-return mission in order to eliminate the effects of the atmosphere on the spectra, and to set constraints on the dust grain sizes.

## Acknowledgments

This work was supported by the European Union's Horizon 2020 research and innovation program (grant agreement No 101004052). Research by O.M. and J.C.G.M. has been partially supported by PID2021-123370OB-100/AEI/10.13039/5011000 11033/FEDER. Research by K.M. and A.P. is supported by the Academy of Finland grants 336546 and 345115.

## Data Availability

The retrieved refractive indices and measured diffuse reflectance spectra will be available at the Granada–Amsterdam Light Scattering Database (www.iaa.es/scattering).

## ORCID iDs

Julia Martikainen https://orcid.org/0000-0003-2211-4001
Olga Muñoz https://orcid.org/0000-0002-5138-3932
Teresa Jardiel https://orcid.org/0000-0002-0163-7324
Juan Carlos Gómez Martín https://orcid.org/0000-0001-7972-085X
Antti Penttilä https://orcid.org/0000-0001-7403-1721
Karri Muinonen https://orcid.org/0000-0001-8058-2642
Gerhard Wurm https://orcid.org/0000-0002-7962-4961

## References

Allen, C. C., Morris, R. V., Lindstrom, D. J., Lindstrom, M. M., & Lockwood, J. P. 1997, LPSC, 28, 27
Arriaga, P., Fitzgerald, M. P., Duchêne, G., et al. 2020, AJ, 160, 79
Cannon, K. M., Britt, D. T., Smith, T. M., Fritsche, R. F., & Batcheldor, D. 2019, Icar, 317, 470
Cantor, B. A., Pickett, N. B., Malin, M. C., et al. 2019, Icar, 321, 161
Christensen, P., & Moore, H. 1992, in The Martian Surface Layer, ed. H. Kieffer (Tucson, AZ: Univ. of Arizona Press), 686
Christensen, P. R. 1986, JGR, 91, 3533
Clancy, R. T., Lee, S. W., Gladstone, G. R., McMillan, W. W., & Rousch, T. 1995, JGR, 100, 5251
Connour, K., Wolff, M. J., Schneider, N. M., et al. 2022, Icar, 387, 115177
Duchêne, G., Rice, M., Hom, J., et al. 2020, AJ, 159, 251
Goetz, W., Pike, W. T., Hviid, S. F., et al. 2010, JGRE, E00E22, 115
Gómez Martín, J. C., Guirado, D., Zubko, E., et al. 2020, JQSRT, 241, 106745
Hansen, J. E., & Travis, L. D. 1974, SSRv, 16, 527
Hapke, B. 2012, Theory of Reflectance and Emittance Spectroscopy (2nd ed.; Cambridge: Cambridge Uni. Press)
Lemmon, M. T., Guzewich, S. D., McConnochie, T., et al. 2019, GeoRL, 46, 9448

Lindqvist, H., Martikainen, J., Räbinä, J., Penttilä, A., & Muinonen, K. 2018, JQSRT, 217, 329
Martikainen, J., Penttilä, A., Gritsevich, M., Lindqvist, H., & Muinonen, K. 2018, JQSRT, 204, 144
Merikallio, S., Nousiainen, T., Kahnert, M., & Harri, A. M. 2013, OExpr, 21, 17972
Muinonen, K. 2004, WRM, 14, 365
Muinonen, K., & Markkanen, J. 2023, in Light, Plasmonics and Particles, ed. M. P. Mengüç & M. Francoeur (Amsterdam: Elsevier), 149
Muinonen, K., Nousiainen, T., Fast, P., Lumme, K., & Peltoniemi, J. I. 1996, JQSRT, 55, 577
Muinonen, K., Nousiainen, T., Lindqvist, H., Muñoz, O., & Videen, G. 2009, JQSRT, 110, 1628
Muñoz, O., Frattin, E., Jardiel, T., et al. 2021, ApJS, 256, 17
Muñoz, O., Volten, H., Hovenier, J. W., et al. 2007, JGRD, 112, D13215
Ockert-Bell, M. E., Bell, J. F., III, Pollack, J. B., McKay, C. P., & Forget, F. 1997, JGR, 102, 9039
Pang, K., Ajello, J., Hord, C., & Egan, W. 1976, Icar, 27, 55
Peters, G. H., Abbey, W., Bearman, G. H., et al. 2008, Icar, 197, 470
Ruff, S. W., & Christensen, P. R. 2002, JGRE, 107, 5127
Shepard, M. K., & Helfenstein, P. 2007, JGRE, 112, E03001
Tomasko, M. G., Doose, L. R., Lemmon, M., Smith, P. H., & Wegryn, E. 1999, JGR, 104, 8987
Weitz, C., Sullivan, R. J., Lapotre, M. G. A., et al. 2018, GeoRL, 45, 9471
Willame, Y., Depiesse, C., Mason, J. P., et al. 2022, P&SS, 218, 105504
Wolff, M. J., Clancy, R. T., Goguen, J. D., Malin, M. C., & Cantor, B. A. 2010, Icar, 208, 143
Wolff, M. J., Smith, M. D., Clancy, R. T., et al. 2006, JGRE, 111, E12S17
Wolff, M. J., Smith, M. D., Clancy, R. T., et al. 2009, JGRE, 114, E00D04